

## Phase-contrast X-ray imaging based on interferometry

Atsushi Momose

Department of Applied Physics, School of Engineering, The University of Tokyo, Hongo 7-3-1, Bunkyo-ku, Tokyo 113-8656, Japan. E-mail: momose@exp.t.u-tokyo.ac.jp

Phase-contrast X-ray imaging including tomographic configuration using a crystal X-ray interferometer is reviewed. The imaging principle based on phase retrieval is described, and some demonstrations showing its high sensitivity are presented on the observations of animal and human cancerous tissues.

**Keywords:** phase contrast; X-ray interferometers; phase retrieval; computed tomography; cancer.

### 1. Introduction

Soon after the discovery of X-rays the importance of the X-ray penetrating property was noticed and X-ray imaging applications have been expanding ever since. The contrast in conventional X-ray transmission images is formed by the difference in the X-ray absorption coefficient, and therefore structures are depicted when X-ray absorbing materials are localizing in an object. For materials consisting of low-Z elements, such as biological soft tissues, however, conventional X-ray imaging is not effective because of the low X-ray absorption coefficient. In order to investigate the structure inside such materials with X-rays, one has to use contrast media containing high-Z elements. When suitable staining procedures cannot be found, few chances of application are given to conventional X-ray imaging.

Recently, research activity using X-ray phase information has been growing remarkably in the field of X-ray imaging. This is because the cross sections of the phase shift of low-Z elements are about 1000 times larger than those of absorption in the hard X-ray region (Momose & Fukuda, 1995). Therefore, X-ray phase contrast can lead us to a breakthrough in biological X-ray imaging. In conventional X-ray imaging, however, X-ray wave nature does not appear, and therefore some devices are needed in X-ray optics to generate contrast caused by the X-ray phase shift. Currently four methods are studied:

- (i) interferometric imaging (Bonse & Hart, 1965a; Ando & Hosoya, 1972; Momose, 1995; Momose & Fukuda, 1995);
- (ii) holography-like imaging under in-line configuration (Snigirev *et al.*, 1995; Wilkins *et al.*, 1996);
- (iii) diffraction enhancement imaging using a crystal (Davis *et al.*, 1995; Ingal & Beliaevskaya, 1995; Chapman *et al.*, 1997);
- (iv) Zernike's phase-contrast microscopy (Schmahel *et al.*, 1994; Kagoshima *et al.*, 2001).

Among these methods, the interferometric imaging reviewed in this article is the most sensitive method to the X-ray phase shift. Although the contrasts generated by the four methods are different from one another, X-ray deflection due to refraction at the sample is commonly related to the mechanisms of contrast generation. In the case of X-ray interferometry, the deflection is detected as interference fringes and the fringe spacing is inversely proportional to the deflection angle. Therefore, the smaller the deflection, the easier is its detection, while other methods prefer a larger deflection to generate stronger contrast. For instance, a 0.1  $\mu\text{rad}$  deflection of 0.1 nm X-rays generates fringes with a 1 mm spacing. On the contrary, when the deflection

is large, interferometry is not suitable because the fringes become too fine to resolve. As a rule, interferometry is therefore suitable for depicting the structures in soft tissues while other methods tend to generate contrast at clear structural boundaries, for instance between tissue and air.

It should also be noted that easy phase retrieval has been achieved by X-ray interferometry and this has enabled quantitative phase imaging. Phase-contrast X-ray computed tomography (CT) (Momose, 1995) has been achieved based on phase retrieval. Its sensitivity is excellent and structures in cancerous rabbit liver (Momose *et al.*, 1995a, 1996; Takeda *et al.*, 2001), rat cerebellum (Momose *et al.*, 1995a; Beckmann *et al.*, 1997) and rat nerve (Bonse *et al.*, 1997) have been revealed by phase-contrast X-ray CT so far. Human cancerous tissues in breast (Momose, Takeda, Itai & Hirano, 1998; Momose, Takeda, Itai, Yoneyama & Hirano, 1998; Takeda *et al.*, 1998), liver (Momose, Takeda, Itai & Hirano, 1998; Takeda, Momose, Yu *et al.*, 2000) and kidney (Momose *et al.*, 1999; Bonse & Beckmann, 2001) have also been demonstrated.

In this article, focusing on biological imaging, the potential of X-ray interferometry and experimental achievements are described.

### 2. Advantage of phase contrast

When X-rays pass an object, the change of the X-ray wave field is expressed by the complex X-ray transmittance  $T(x, y) = |T(x, y)| \exp[i\Phi(x, y)]$ .  $|T(x, y)|$  is given by

$$|T(x, y)|^2 = \exp\left[-\int \mu(x, y, z) dz\right], \quad (1)$$

where  $\mu(x, y, z)$  is the linear absorption coefficient and the X-ray propagation direction is assumed to be parallel to the  $z$ -axis. In quantitative measurements like CT, the optical density,

$$D(x, y) = -\log |T(x, y)|^2 = \int \mu(x, y, z) dz, \quad (2)$$

is evaluated. The phase shift  $\Phi(x, y)$  is given by

$$\Phi(x, y) = (2\pi/\lambda) \int \delta(x, y, z) dz, \quad (3)$$

where  $\lambda$  is the X-ray wavelength and  $\delta(x, y, z)$  is the refractive index decrement from unity.

$\mu(x, y, z)$  and  $\delta(x, y, z)$  are written using atomic parameters as

$$\mu(x, y, z) = \sum_k N_k(x, y, z) \mu_k^a \quad (4)$$

and

$$\delta(x, y, z) = (r_e \lambda^2 / 2\pi) \sum_k N_k(x, y, z) (Z_k + f_k'), \quad (5)$$

where  $N_k(x, y, z)$ ,  $\mu_k^a$ ,  $Z_k$  and  $f_k'$  are the atomic density, atomic absorption coefficient (cross section), atomic number and the real part of the anomalous atomic scattering factor of element  $k$ , and  $r_e$  is the classical electron radius. The substitutions of (4) into (2) and (5) into (3) yield

$$D(x, y) = \int \sum_k N_k(x, y, z) \mu_k^a dz \quad (6)$$

and

$$\Phi(x, y) = \int \sum_k N_k(x, y, z) p_k dz, \quad (7)$$

where

$$p_k \equiv r_e \lambda (Z_k + f_k'), \quad (8)$$

which is defined for comparison with the absorption cross section  $\mu_k^a$ ; that is,  $p_k$  by analogy corresponds to the cross section of the X-ray phase shift. By comparing (6) and (7) it can be seen that the density

and composition contribute in the same manner and the difference is attributed to  $p$  and  $\mu^a$ . Therefore, the advantage of detecting the phase shift over detecting the absorption is discussed by graphing  $p$  and  $\mu^a$  as functions of the atomic number as shown in Fig. 1. Curves for 5, 10, 20 and 40 keV monochromatic X-rays are shown. The values of  $\mu_k^a$  and  $f_k'$  from public tables (Sasaki, 1989, 1990) are used.

It should be noted that  $p$  is always larger than  $\mu^a$  and, especially for low- $Z$  elements, the ratio  $p/\mu^a$  is about 1000. This means that remarkable improvement in sensitivity is achieved by using X-ray phase information in the imaging of soft tissues. In addition, the high sensitivity contributes to reducing X-ray radiation damage, which is important in biological X-ray imaging.

### 3. X-ray interferometer

As shown in Fig. 2, an X-ray interferometer is made from a silicon perfect crystal, and transmission-type (Laue-case) diffraction by crystal lamellae is used to divide and combine the X-ray wave field coherently (Bonse & Hart, 1965*b*). The configuration, having three lamellae at regular intervals as shown in Fig. 2, is typical, and is called a triple Laue-case (LLL) interferometer. The first lamella divides the incident beam into two beams, which are inclined by  $2\theta_B$  to each other, where  $\theta_B$  is the Bragg diffraction angle. The two beams are spatially separated at the centre lamella and divided into two. Among the thus-generated four beams, the two propagating inside overlap coherently at the third lamella. Each beam is again divided into two, and interference occurs in the outgoing beams. This configuration corresponds to the Mach-Zehnder interferometer.

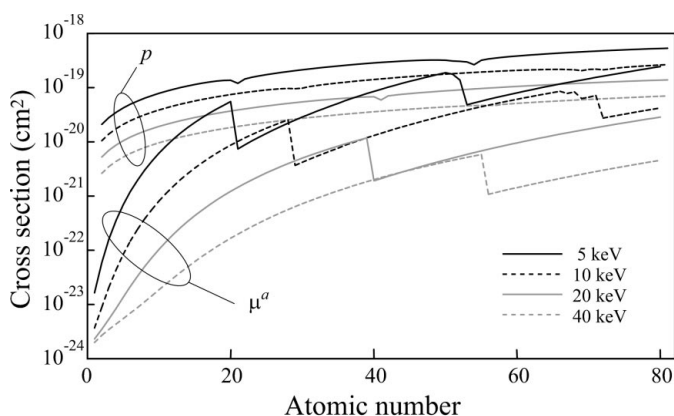


**Figure 1**  
Cross sections of the X-ray phase shift and absorption ( $p$  and  $\mu^a$ ) as a function of the atomic number.

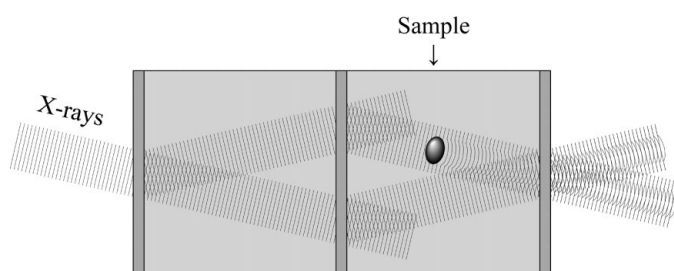


**Figure 2**  
Triple Laue-case (LLL) X-ray interferometer and beam paths.

The LLL interferometer is normally fabricated by cutting the entire body monolithically out of an ingot of floating zone silicon crystal. Then, the interferometer is considered to be a single crystal, and no mechanical tuning is required except for setting the angle of incident X-rays to the Bragg condition. When an X-ray interferometer is composed of independent lamellae, extremely high precision is required in its alignment mechanism so that the optical path length is stable within a deviation smaller than the X-ray wavelength. Nevertheless, such a non-monolithic configuration is also studied for phase-contrast X-ray imaging of a large field of view (Yoneyama *et al.*, 1999).

The high sensitivity of X-ray interferometry to biological soft tissues was demonstrated with a slice of a rat cerebellum (Momose & Fukuda, 1995). Fig. 3(*a*) shows an interference pattern of a slice obtained on an X-ray film (Fuji #50) with 12.4 keV synchrotron radiation X-rays at the Photon Factory, Tsukuba, Japan. Contrast showing white matter, a granular layer, and a molecular layer was revealed. For comparison, a corresponding absorption-contrast image was measured with the same exposure by blocking the reference beam with a lead plate as shown in Fig. 3(*b*), where no structure could be depicted.

This demonstration, however, was performed under the simplest usage of the X-ray interferometer, and quantitative understanding of the sample was not easy. Phase-retrieval techniques described in the

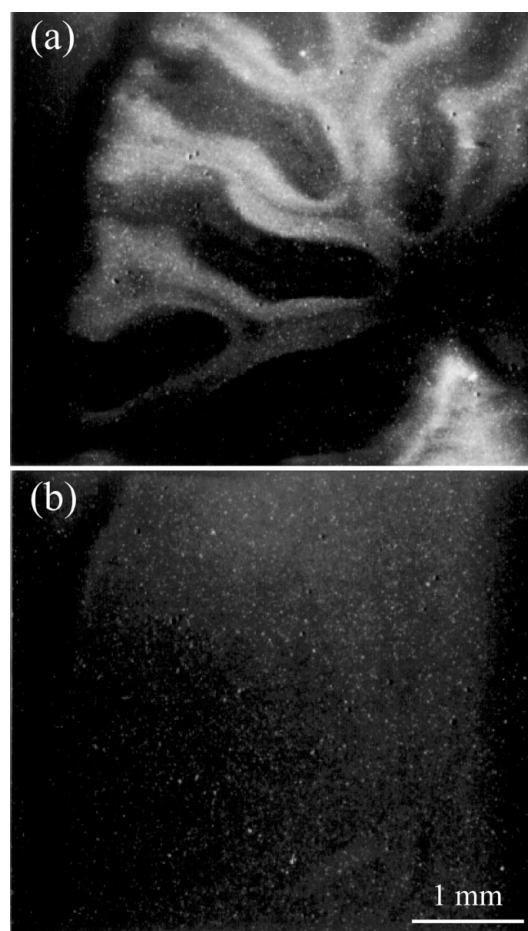


**Figure 3**  
Interference pattern (*a*) and corresponding absorption-contrast image (*b*) of a slice of rat cerebellum. Both images were obtained with the same dose of X-rays (12.4 keV).

following section opened up a new possibility of a more sophisticated usage of the X-ray interferometer.

#### 4. Imaging principle

##### 4.1. Phase retrieval

An interference pattern  $I(x, y)$  generated by the X-ray interferometer is given in general by

$$I(x, y) = a(x, y) + b(x, y) \cos[\Phi(x, y) + \Delta(x, y)], \quad (9)$$

where  $a(x, y)$  and  $b(x, y)$  are the average intensity and fringe amplitude, and  $\Phi(x, y)$  and  $\Delta(x, y)$  are the phase shift caused by a sample given by (3) or (7) and the inherent phase background owing to the imperfection of the X-ray interferometer. Thus, even when no sample is placed in the beam [ $\Phi(x, y) = 0$ ], interference fringes (built-in Moiré fringes) appear normally.

For a quarter of a century since the invention of the LLL interferometer by Bonse and Hart, phase-contrast imaging was performed with it simply by taking a picture of an interference pattern (Bonse & Hart, 1965*b*; Ando & Hosoya, 1972). Because the existence of  $\Delta(x, y)$  in (9) is crucial in such a case, an almost complete interferometer was required for imaging. Furthermore, samples should be sliced with a constant thickness to prevent fringes from appearing due to thickness variation.

In the hard X-ray energy region, two methods for phase retrieval, *i.e.* the determination of  $\Phi(x, y)$  from interference patterns expressed in (9), are applicable with the LLL interferometer. One is the fringe-scanning method (Bruning *et al.*, 1974) and the other is the Fourier transform method (Takeda *et al.*, 1982). The techniques of phase retrieval have enabled flexible phase-contrast X-ray imaging using the LLL interferometer, even if the interferometer is not complete. Quantitative analysis became possible and this led to the achievement of phase-contrast X-ray CT described later.

##### 4.2. Fringe-scanning method

This method, which is also known as phase-shifting interferometry, requires the measurement of several interference patterns by changing the phase difference between the reference and object beams. When  $M$  interference patterns are measured varying the phase difference with a step of  $2\pi/M$ , each interference pattern is given by

$$I_k(x, y) = a(x, y) + b(x, y) \cos[\Phi(x, y) + \Delta(x, y) + 2\pi k/M], \quad (10)$$

where  $k = 1, 2, \dots, M$ . Here, the summation  $S(x, y)$  of  $I_k(x, y)$  with a weight of  $\exp(-2\pi i k/M)$  yields

$$\begin{aligned} S(x, y) &= \sum_{k=1}^M I_k(x, y) \exp(-2\pi i k/M) \\ &= (1/2) M b(x, y) \exp\{i[\Phi(x, y) + \Delta(x, y)]\}, \end{aligned} \quad (11)$$

for  $M > 3$ . Therefore,  $\Phi(x, y) + \Delta(x, y)$  is given by

$$\Phi(x, y) + \Delta(x, y) = \tan^{-1} \{ \text{Im}[S(x, y)] / \text{Re}[S(x, y)] \}. \quad (12)$$

Because  $\Delta(x, y)$  can be determined in the absence of a sample in advance, (12) can give  $\Phi(x, y)$ . Amplitude information is carried in  $b(x, y)$  and extracted by calculating  $|S(x, y)|$ .

##### 4.3. Fourier transform method

This method gives  $\Phi(x, y)$  from a single interference pattern by introducing carrier fringes with a constant spacing. Then, the interference pattern is given by

$$I(x, y) = a(x, y) + b(x, y) \cos[\Phi(x, y) + \Delta(x, y) + 2\pi f_o x], \quad (13)$$

where  $f_o$  is the carrier frequency in the direction of  $x$ . For explanation purposes, (13) is rewritten as

$$I(x, y) = a(x, y) + c(x, y) \exp(2\pi i f_o x) + c^*(x, y) \exp(-2\pi i f_o x), \quad (14)$$

where

$$c(x, y) = (1/2) b(x, y) \exp\{i[\Phi(x, y) + \Delta(x, y)]\} \quad (15)$$

and the asterisk denotes the complex conjugate.

The Fourier transform of (14) with respect to  $x$  is given by

$$I_F(f, y) = a_F(f, y) + c_F(f - f_o, y) + c_F^*(f + f_o, y), \quad (16)$$

where the subscript  $F$  indicates the Fourier transform of each term in (14). If structures of spatial frequency much higher than  $f_o$  are not contained in  $a$ ,  $b$  and  $\Phi$ , the peaks corresponding to each term of (16) do not overlap. Therefore, the peak corresponding to the second or the third term can be extracted. When the peak of the second term, for instance, is extracted and translated to the origin, one can obtain  $c_F(f, y)$ . This translation means the removal of the carrier fringes. The inverse Fourier transform of  $c_F(f, y)$  with respect to  $f$  gives  $c(x, y)$ . Then, similar to (12),  $\Phi(x, y) + \Delta(x, y)$  is given by

$$\Phi(x, y) + \Delta(x, y) = \tan^{-1} \{ \text{Im}[c(x, y)] / \text{Re}[c(x, y)] \}. \quad (17)$$

The advantage of this method is that  $\Phi(x, y)$  is obtained rapidly while the fringe-scanning method requires a longer time. However, one needs to compromise that structures smaller than the carrier fringe spacing cannot be resolved, while the fringe-scanning method is free from this problem. This limitation is attributed to the assumption that the peaks corresponding to each term of (16) are separated.

##### 4.4. Phase unwrapping

Equations (12) and (17) contain an arctangent operation whose value ranges from  $-\pi$  to  $\pi$ . Therefore, when  $\Phi(x, y)$  exceeds  $2\pi$ , jumps of  $2\pi$  are contained inevitably in a resultant image. Such an image is called a wrapped phase map (Fig. 4*a*) and phase unwrapping implies compensating the jumps to obtain a real phase map.

When the phase shift is varying smoothly, the phase jump is easily detected because a phase difference near  $2\pi$  is found between neighbouring pixels. The jump can be removed by repeating addition or subtraction of  $2\pi$  to or from one of the neighbouring pixels.

However, when the signal-to-noise ratio of an image is low or when abrupt phase variation exists, one fails in phase unwrapping occasionally because the phase jump becomes partially unclear. To overcome this problem, the so-called cut-line algorithm (Huntley, 1989) is used. The cut-line algorithm detects unclear jumps automatically and sets cut-lines there to inhibit unwrapping across the cut-

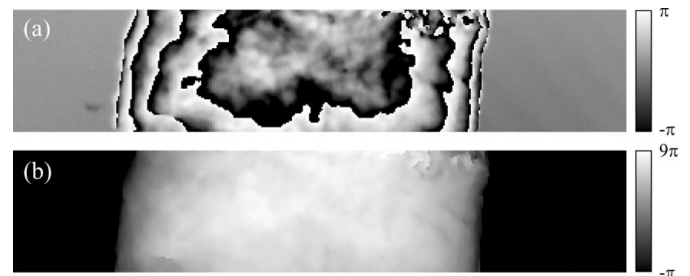


**Figure 4** Wrapped phase map (a) and unwrapped phase map (b) using the cut-line algorithm.

lines. Then, an almost consistent phase map is reproduced even if an image contains some defects (Fig. 4b).

#### 4.5. Tomographic three-dimensional reconstruction

In general, when a function  $G$  is expressed with a projection form of a scalar function  $F$  describing three-dimensional sample structure, CT can determine  $F$  from  $G$  measured in multiple projection directions. In the case of CT with monochromatic X-rays, equation (2) corresponds to the projection relation, and tomograms mapping the linear absorption coefficient are reconstructed. Equation (3) also satisfies this relation, and this means that the phase-retrieval technique enables the reconstruction of a tomographic image mapping the refractive index. This concept of phase-contrast X-ray computed tomography was demonstrated (Momose, 1995) by repeating the measurement of the phase map with the fringe-scanning method while rotating the sample.

As suggested in Fig. 1, the sensitivity to soft tissues of phase-contrast X-ray CT is expected to be about 1000 times higher than that of absorption-contrast X-ray CT that uses monochromatic X-rays. However, this is true on the assumption that the error  $\Delta\Phi$  in the phase retrieval caused by photon statistics is  $\sim N^{-1/2}$ , where  $N$  is the total number of X-ray photons per pixel per phase map, because  $\Delta D$  is also  $\sim N^{-1/2}$  in absorption-contrast X-ray CT. It can be shown from (11) and (12) that the fringe-scanning method meets this requirement.

### 5. Experiment

#### 5.1. Apparatus

The apparatus for phase-contrast X-ray imaging (Momose *et al.*, 1998b) is shown in Fig. 5. Synchrotron radiation from a vertical wiggler at the Photon Factory through a double-crystal monochromator was expanded by asymmetric diffraction and introduced into the LLL interferometer. A plastic plate (0.5 mm thick) was used to apply the fringe-scanning method; the phase of the reference beam

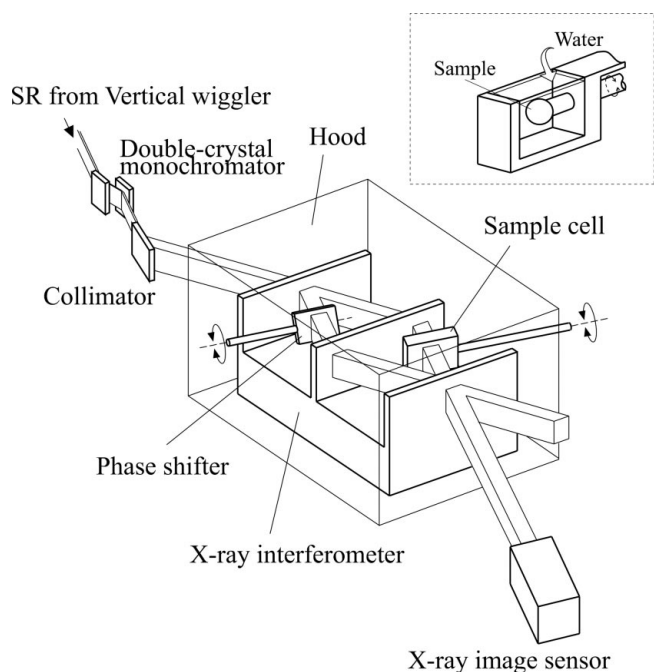


**Figure 5**  
Experimental set-up using the X-ray interferometer.

was changed by rotating the plate. A sample was put into a cell filled with liquid. Therefore, a wet sample could be imaged flexibly. A more important advantage of using the cell was that the refraction at the sample surface was moderately reduced. Otherwise, when a sample was placed in air, interference fringes occasionally became too narrow to resolve. For phase-contrast X-ray CT, the sample was rotated in the cell. The interferometer was covered with a hood and the whole apparatus was also covered with another large hood to prevent airflow from causing deformation of the interferometer. Interference images were detected with an X-ray sensing pick-up tube (Suzuki *et al.*, 1989). The size of a pixel was tunable, and  $12\ \mu\text{m} \times 12\ \mu\text{m}$  or  $12\ \mu\text{m} \times 18\ \mu\text{m}$  was typical.

#### 5.2. Phase map measurement – blood contrast

An example of phase map measurement is described below. This experiment (Momose *et al.*, 2001) was carried out to demonstrate that blood itself generates phase contrast. In clinical vascular imaging, contrast agents containing a high- $Z$  element are injected into blood vessels, otherwise no absorption contrast is generated by the blood vessels. On the other hand, because the refractive index of blood is significantly different from that of the surrounding tissue, it was expected that blood would generate phase contrast without using contrast agents (Momose *et al.*, 1995b).

The experiment was performed using a mouse liver, which was excised just before measurement by tying the portal vein, hepatic artery and hepatic vein to prevent blood from flowing out of the liver. The excised liver was placed in a cell filled with physiological salt solution. Fig. 6 shows a phase map obtained with 17.7 keV X-rays with a five-step fringe scan. The total exposure was  $5 \times 10^7$  photons  $\text{mm}^{-2}$ . The field of view was  $13\ \text{mm} \times 9\ \text{mm}$  using a large LLL interferometer (Takeda, Momose, Hirano *et al.*, 2000). In producing Fig. 6, contrast caused by thickness variation of the liver was removed by image processing. Trees of blood vessels were revealed, and vessels with a diameter of about  $50\ \mu\text{m}$  could be detected.

#### 5.3. Phase-contrast X-ray CT

Fig. 7 shows a three-dimensional rendering view of phase-contrast X-ray CT data obtained for a column piece of a rabbit liver with VX2 cancer using 17.7 keV X-rays (Momose *et al.*, 1996). The sample was placed in a cell filled with water and rotated with a  $0.9^\circ$  step over  $180^\circ$ . At every angular position, a phase map was measured with a ten-step fringe scan. The voxel size was  $12\ \mu\text{m} \times 12\ \mu\text{m} \times 12\ \mu\text{m}$ . The cancer lesion (left half) appeared dark and is easily distinguishable from the

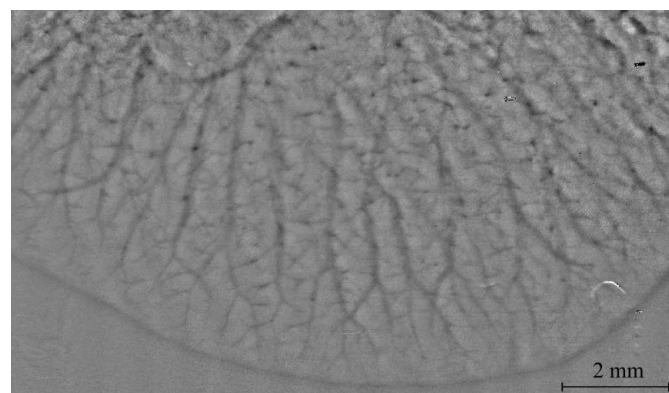


**Figure 6**  
Phase map obtained for a mouse liver. Trees of blood vessels are depicted because of the phase contrast caused by blood.

normal tissue (right half). Furthermore, structures in the tumor are also detected; bright regions correspond to necrosis. Human tissues were also investigated using this method, and Fig. 8 shows an example obtained with the same measurement condition for a cancerous tissue of human kidney (Momose *et al.*, 1999). The cancerous lesion (right half) is also differentiated from the normal.

As suggested from (5),  $\delta$  is approximately proportional to the density of an electron (note  $f' \ll Z$ ). Furthermore, especially for low- $Z$  elements, it is proportional to mass density. Therefore, a phase-contrast X-ray CT image is understood as a map of mass density. According to the signal-to-noise ratio of actually obtained phase-contrast CT images, the detection limit of the density deviation was  $4 \text{ mg cm}^{-3}$  (Momose *et al.*, 1996).

## 6. Perspectives

The excellent sensitivity of X-ray interferometry to soft tissues has been well demonstrated on various tissues. However, some technical

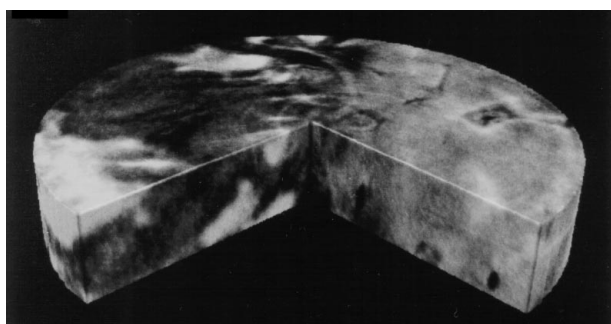


**Figure 7**  
Three-dimensional rendering view of phase-contrast X-ray CT data obtained for a tissue piece (5 mm in diameter) of rabbit liver with VX2 cancer (Momose *et al.*, 1996). The dark area corresponds to a cancerous lesion and necrosis is detected as bright islands in the tumor.

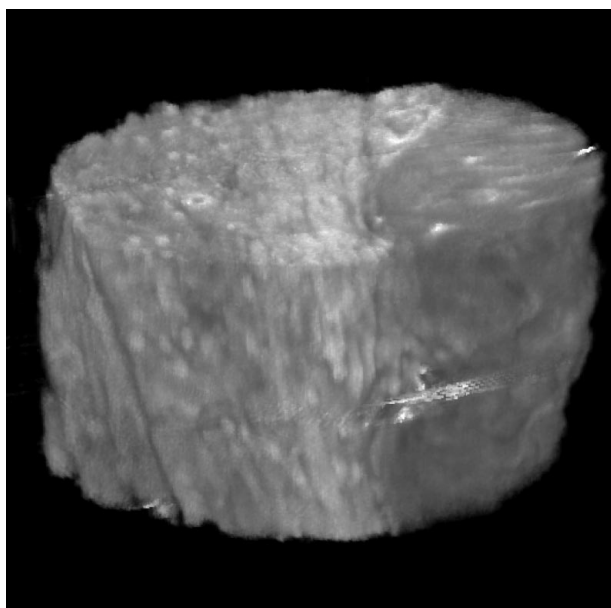


**Figure 8**  
Three-dimensional rendering view of phase-contrast X-ray CT data obtained for a tissue piece (10 mm in diameter) of human cancerous kidney (Momose *et al.*, 1999).

problems should still be overcome for future applications, as discussed below.

### 6.1. Field of view

The performance of phase-contrast X-ray imaging is attractive from a medical point of view. However, especially for clinical purposes, the field of view provided by the monolithic LLL interferometer is insufficient, because the LLL interferometer is cut out monolithically from an ingot of floating zone silicon crystal, the diameter of which is 15 cm at its maximum. Although a field of view of about  $7 \text{ cm} \times 7 \text{ cm}$  can be generated according to geometrical considerations, it is still insufficient for clinical diagnostics.

In order to generate a larger field of view, a non-monolithic LLL interferometer should be studied. As mentioned, however, because the advantage of the monolithic configuration is relinquished, an alignment mechanism with extremely high precision is required so that the optical path length is sufficiently stabilized compared with the X-ray wavelength.

One candidate is the skew-symmetric configuration (Becker & Bonse, 1974) consisting of two independent crystal blocks, each of which has two lamellae, as shown in Fig. 9. This configuration has the advantage that the displacement of one block against the other does not affect interference. Consequently, the interferometer can be aligned by tuning two rotation axes ( $\rho$  and  $\theta$ ). Detuning of  $\rho$  causes rotation Moiré fringes, and a normal tilt stage is available to tune the  $\rho$  axis. One needs to concentrate on tuning the  $\theta$  axis, the detuning of which causes a phase difference between the two arms of the interferometer. The phase difference  $\Phi'$  is given by

$$\Phi' \simeq 2\pi x \Delta\theta / d, \quad (18)$$

where  $x$  and  $d$  are the spacing between the two lamellae and the Bragg plane spacing, respectively. Assuming that  $x = 100 \text{ nm}$  and Si 220 diffraction is used,  $\Delta\theta$  should be below 1 nrad to keep  $\Phi'$  under  $2\pi$ .

Thus, operation of the skew-symmetric two-crystal interferometer is very challenging, especially at synchrotron radiation facilities where disturbances like vibration are assumed to exist. As a result, a system is successfully operated where sleeve-bearing mechanisms and a feedback control are adopted. The system is installed at the vertical wiggler beamline of the Photon Factory, and the generation of a  $25 \text{ mm} \times 15 \text{ mm}$  field of view and demonstrations of phase-contrast X-ray imaging have been achieved (Yoneyama *et al.*, 1999). The vertical wiggler is convenient for this system because a fan beam spreading in the vertical direction is available. Then, a wide beam is created with a single asymmetric diffraction and interferometer arms can be formed in a horizontal plane; this configuration is advantageous in building a rigid system. The next version of a  $30 \text{ mm} \times 30 \text{ mm}$  field of view is under development. If a  $10 \text{ cm} \times 10 \text{ cm}$  field of view is generated in the future, phase-contrast mammography might be achieved.

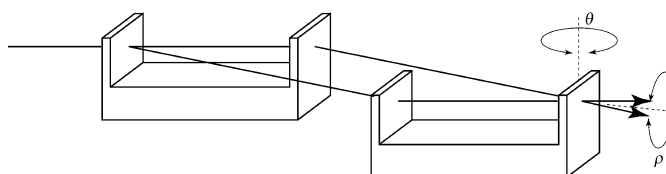


**Figure 9**  
Configuration of the non-monolithic X-ray interferometer.

## 6.2. Spatial resolution

Microscopic applications of the present technique are also attractive. However, one needs to overcome a problem in spatial resolution: it was pointed out that the lamella located between a sample and an image sensor limits the spatial resolution (Momose & Hirano, 1999). The function of the lamella as an X-ray half mirror is described by the dynamical X-ray diffraction theory, according to which X-ray propagation direction inside the lamella varies sensitively to the change of the angle of incident X-rays. The deviation in the incident angle is roughly amplified by  $10^4$  in a crystal. Because a sample causes refraction, which is the origin of the generation of interference fringes, the incident angle is not homogeneous. As a result, the refraction at a sample causes image blurring.

To reduce the blurring, various techniques have been employed or studied:

(i) Putting the sample in liquid, as mentioned above. Then, the change of the refractive index at the sample surface is moderately reduced, and too strong refraction is avoided.

(ii) For phase-contrast X-ray CT, setting the sample rotation axis parallel to the scattering plane (the plane spanned by beam paths) as shown in Fig. 5. Then, sectional images are reconstructed on the planes perpendicular to the scattering plane. Because the refraction in the direction perpendicular to the scattering plane is independent of the blurring effect, the reduction of the spatial resolution is minimized.

(iii) Thinning the lamella. Improvement in the spatial resolution has been demonstrated using an LLL interferometer with a  $240\ \mu\text{m}$  lamella (Hirano & Momose, 1999) or a  $180\ \mu\text{m}$  lamella (Momose *et al.*, 2001). The use of reflection-type (Bragg case) diffraction is also studied (Yoneyama *et al.*, 2002); configurations such that X-rays through a sample do not transmit but reflect at a crystal are realised. By such efforts, a spatial resolution of a few  $\mu\text{m}$  is expected in phase-contrast X-ray CT not only for biological tissues but also for inorganic materials.

## 6.3. Others

Acquisition of a phase-map movie is also attractive. However, all phase-map-imaging experiments are currently performed under static conditions. Although it is easy to record a movie of the interference image at third-generation synchrotron facilities, acquisition of a phase-map movie has never been achieved because at least three interference images are needed to obtain a phase map by using the fringe-scanning method. One approach is to use the Fourier trans-

form method if the spatial resolution can be compromised. The other is by performing a quick fringe scan, for which the author is developing a phase shifter synchronizing with frame transfer of an X-ray image sensor. With this equipment, phase-map measurement would be speeded up and then 1 min scan phase-contrast X-ray CT might be achieved.

One can find an optimal X-ray energy depending on the thickness of a sample minimizing the X-ray dose for a given sensitivity (Momose *et al.*, 1997). Therefore, X-ray interferometry with X-rays of higher energy should be studied for investigating thick objects, especially when clinical applications are attempted.

In addition, phase contrast at the resonant energy (absorption edge) is attractive because the phase shift is varied depending on the density and chemical state of a specific element. In the hard X-ray energy region, mapping of metals in depicted soft structures would be attractive. Provided a soft X-ray interferometer is developed, one can access the resonant energies of low- $Z$  elements. Fig. 10 shows  $p$  and  $\mu^a$  for carbon as a function of X-ray energy. Although the advantage of phase contrast is thus not conspicuous in the soft X-ray region, it should be noted that  $p$  varies tremendously at the  $K$  edge and its value is negative and out of the range of Fig. 10. The author is developing an interferometer using self-standing thin films.

## 7. Conclusions

The cross section of the X-ray phase shift is about 1000 times larger than that of absorption for low- $Z$  elements, and X-ray interferometry provides a way of taking advantage of it by 100% in phase-contrast X-ray imaging. Mapping of the phase shift is achieved and tomographic image reconstruction is also demonstrated for various biological soft tissues. Aiming at medical applications, a large X-ray interferometer under a non-monolithic configuration has been developed at the Photon Factory. Some other improvements towards real-time observation and phase-contrast microtomography are also in progress.

Present experiments using synchrotron radiation were carried out under proposal numbers 93-Y003, 94-G144, 95-Y005, 97-G164 and 99S2-002 approved by the High Energy Accelerator Research Organization. Part of this study was supported through Special Coordination Funds of the Science and Technology Agency of the Japanese Government.

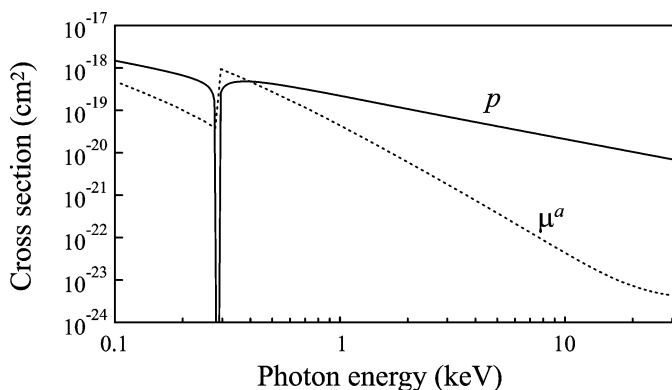


**Figure 10**  
Cross sections of the X-ray phase shift and absorption ( $p$  and  $\mu^a$ ) of carbon as a function of X-ray energy.

## References

- Ando, M. & Hosoya, S. (1972). *Proceedings of the 6th International Conference on X-ray Optics and Microanalysis*, edited by G. Shinoda, K. Kohra & T. Ichinokawa, pp. 63–68. Tokyo: University Tokyo Press.
- Becker, P. & Bonse, U. (1974). *J. Appl. Cryst.* **7**, 593–598.
- Beckmann, F., Bonse, U., Busch, F. & Günnewig, O. (1997). *J. Comput. Assist. Tomogr.* **21**, 539–553.
- Bonse, U. & Beckmann, F. (2001). *J. Synchrotron Rad.* **8**, 1–5.
- Bonse, U., Beckmann, F., Bartscher, M., Biermann, T., Busch, F. & Günnewig, O. (1997). *Proc. SPIE*, **3149**, 108–119.
- Bonse, U. & Hart, M. (1965a). *Appl. Phys. Lett.* **7**, 99–101.
- Bonse, U. & Hart, M. (1965b). *Appl. Phys. Lett.* **6**, 155–156.
- Bruning, J. H., Herriott, D. R., Gallagher, J. E., Rosenfeld, D. P., White, A. D. & Brangaccio, D. J. (1974). *Appl. Opt.* **13**, 2693–2703.
- Chapman, D., Thomlinson, W., Johnston, R. E., Washburn, D., Pisano, E., Gmür, N., Zhong, Z., Menk, R., Arfelli, F. & Sayers, D. (1997). *Phys. Med. Bio.* **42**, 2015–2025.

- Davis, J., Gao, D., Gureyev, T. E., Stevenson, A. W. & Wilkins, S. W. (1995). *Nature (London)*, **373**, 595–598.
- Hirano, K. & Momose, A. (1999). *Jpn. J. Appl. Phys.* **38**, L1556–L1558.
- Huntley, J. M. (1989). *Appl. Opt.* **28**, 3268–3270.
- Ingal, V. N. & Beliaevskaya, E. A. (1995). *J. Phys. D.* **28**, 2314–2317.
- Kagoshima, Y., Ibaki, T., Yokoyama, Y., Tsusaka, Y., Mitsui, J., Takai, K. & Anio, M. (2001). *Jpn. J. Appl. Phys.* **40**, L1190–L1192.
- Momose, A. (1995). *Nucl. Instrum. Methods A*, **352**, 622–628.
- Momose, A. & Fukuda, J. (1995). *Med. Phys.* **22**, 375–380.
- Momose, A. & Hirano, K. (1999). *Jpn. J. Appl. Phys. Suppl.* **38**(1), 625–629.
- Momose, A., Koyama, I. & Hirano, K. (2001). *Proc. SPIE*, **4503**, 71–81.
- Momose, A., Takeda, T. & Itai, Y. (1995a). *Rev. Sci. Instrum.* **66**, 1434–1436.
- Momose, A., Takeda, T. & Itai, Y. (1995b). *Acad. Radiol.* **2**, 883–887.
- Momose, A., Takeda, T. & Itai, Y. (1996). *Nature Medicine* **2**, 473–475.
- Momose, A., Takeda, T. & Itai, Y. (1997). *Proc. SPIE*, **3149**, 120–129.
- Momose, A., Takeda, T. & Itai, Y. (2001). *Radiology*, **217**, 593–596.
- Momose, A., Takeda, T., Itai, Y. & Hirano, K. (1998). *X-ray Microscopy and Spectromicroscopy*, edited by J. Thieme, G. Schmahl, D. Rudolph & E. Umbach, pp. II207–II212, Berlin: Springer-Verlag.
- Momose, A., Takeda, T., Itai, Y., Tu, J. & Hirano, K. (1999). *Proc. SPIE*, **3659**, 365–374.
- Momose, A., Takeda, T., Itai, Y., Yoneyama, A. & Hirano, K. (1998). *J. Synchrotron Rad.* **5**, 309–314.
- Sasaki, S. (1989). *KEK Report 88-14*. National Laboratory for High Energy Physics, Tsukuba, Japan.
- Sasaki, S. (1990). *KEK Report 90-16*. National Laboratory for High Energy Physics, Tsukuba, Japan.
- Schmahl, G., Gutmann, P., Schneider, G., Niemann, B., David, C., Wilhein, T., Thieme, J. & Rudolph, D. (1994). *X-ray Microscopy IV*, edited by V. V. Aristov & A. I. Erko, pp. 196–206. Moscow: Bogorodskii Pechatnik.
- Snigireva, I., Kohn, V., Kuznetsov, S. & Schelokov, I. (1995). *Rev. Sci. Instrum.* **66**, 5486–5492.
- Suzuki, Y., Hayakawa, K., Usami, K., Hirano, T., Endoh, T. & Okamura, Y. (1989). *Rev. Sci. Instrum.* **60**, 2299–2302.
- Takeda, M., Ina, H. & Kobayashi, S. (1982). *J. Opt. Soc. Am.* **72**, 156–160.
- Takeda, T., Momose, A., Hirano, K., Haraoka, S., Watanabe, T. & Itai, Y. (2000). *Radiology*, **214**, 298–301.
- Takeda, T., Momose, A., Wu, J., Zeniya, T., Yu, Q., Lwin, T.-T., Yoneyama, A. & Itai, Y. (2001). *Nucl. Instrum. Methods A*, **467/468**, 1322–1325.
- Takeda, T., Momose, A., Ueno, E. & Itai, Y. (1998). *J. Synchrotron Rad.* **5**, 1133–1135.
- Takeda, T., Momose, A., Yu, Q., Wu, J., Hirano, K. & Itai, Y. (2000). *J. Synchrotron Rad.* **7**, 280–282.
- Wilkins, S. W., Gureyev, T. E., Gao, D., Pogany, A. & Stevenson, A. W. (1996). *Nature (London)*, **384**, 335–338.
- Yoneyama, A., Momose, A. & Koyama, I. (2002). *Jpn. J. Appl. Phys.* **41**, L161–L163.
- Yoneyama, A., Momose, A., Seya, E., Hirano, K., Takeda, T. & Itai, Y. (1999). *Rev. Sci. Instrum.* **70**, 4582–4586.